

# Robust Depth Super-Resolution via Adaptive Diffusion Sampling

Kun Wang<sup>1</sup> Yun Zhu<sup>2</sup> Pan Zhou<sup>3</sup> Na Zhao<sup>1</sup>

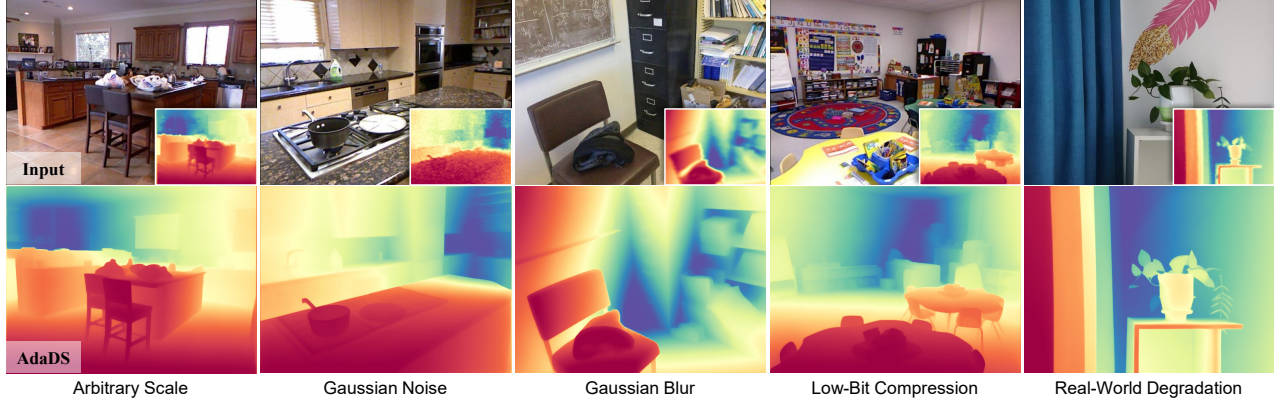


Figure 1. We introduce **AdaDS**, a framework designed to address the persistent generalization challenges in depth super-resolution problem. Given an arbitrarily degraded low-resolution depth map and its corresponding RGB image, AdaDS employs zero-shot inference to reconstruct a high-resolution metric depth map with fine-grained structural details.

## Abstract

We propose AdaDS, a generalizable framework for depth super-resolution that robustly recovers high-resolution depth maps from arbitrarily degraded low-resolution inputs. Unlike conventional approaches that directly regress depth values and often exhibit artifacts under severe or unknown degradation, AdaDS capitalizes on the contraction property of Gaussian smoothing: as noise accumulates in the forward process, distributional discrepancies between degraded inputs and their pristine high-quality counterparts diminish, ultimately converging to isotropic Gaussian prior. Leveraging this, AdaDS adaptively selects a starting timestep in the reverse diffusion trajectory based on estimated refinement uncertainty, and subsequently injects tailored noise to position the intermediate sample within the high-probability region of the target posterior distribution. This strategy ensures inherent robustness, enabling generative prior of a pre-trained diffusion model to dominate recovery even when upstream esti-

mations are imperfect. Extensive experiments on real-world and synthetic benchmarks demonstrate AdaDS’s superior zero-shot generalization and resilience to diverse degradation patterns compared to state-of-the-art methods.

## 1. Introduction

Depth super-resolution (DSR) constitutes a vital component of monocular 3D perception (Wang et al., 2024a; Fan et al., 2025; Yan et al., 2025b). The task seeks to reconstruct an accurate, high-resolution depth map from a coarse, low-resolution measurement, guided by a corresponding high-resolution RGB image. By integrating rich semantic cues from readily accessible color images with metric priors from cost-effective range sensors (*e.g.* Time-of-Flight (ToF) cameras and structured-light systems), DSR effectively mitigates the scale and geometric ambiguities inherent in monocular depth estimation. Consequently, it substantially reduces the cost of acquiring high-quality depth data, thereby bolstering performance in a wide range of downstream applications, including 3D scene reconstruction (Chung et al., 2024; Wang et al., 2024b), AR/VR (Holynski & Kopf, 2018; Du et al., 2020), and robotics (Dong et al., 2022; Sheng et al., 2023).

In recent years, numerous DSR methods have emerged, achieving remarkable results under controlled settings, such as fixed upsampling factors, specific scene types, and limited

<sup>1</sup>IMPL, Singapore University of Technology and Design <sup>2</sup>PCA Lab, Nanjing University of Science and Technology <sup>3</sup>LV-Lab, Singapore Management University. Correspondence to: Kun Wang <kun\_wang@sutd.edu.sg>, Na Zhao <na\_zhao@sutd.edu.sg>.

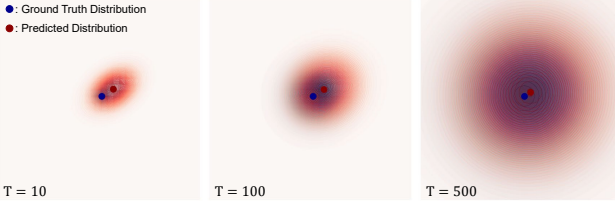


Figure 2. The distribution of the degraded input (with predicted mean and variance from coarse refinement) progressively aligns with the ground-truth distribution due to Gaussian smoothing contraction. Dots indicate the means of the 2D Gaussians.

degradation patterns (Shi et al., 2022; Zhong et al., 2023; Wang et al., 2024c). However, robustness remains a critical limitation that hinders their practical deployment. Real-world depth inputs, acquired from hardware-constrained sensors, often exhibit complex and unpredictable degradations. As a result, most existing approaches suffer from substantial performance drops due to domain discrepancies, failing to reliably recover fine-grained, accurate depth maps in diverse real-world scenarios.

To address this challenge, we propose AdaDS that robustly handles arbitrary degradation patterns. Unlike conventional methods that rely on direct regression of depth values, which often struggle with severe or unseen degradations, AdaDS innovatively incorporates the high-quality depth distribution prior implicit in pre-trained diffusion models (Ho et al., 2020). Our *key insight* is that the forward diffusion process progressively erases distributional discrepancies between degraded low-resolution inputs and their pristine high-quality counterparts via Gaussian smoothing contraction, converging both to a shared isotropic Gaussian (see the 2D Gaussian analogy in Fig. 2). This implies the existence of an optimal timestep that balances fidelity to the input content with sufficient alignment to the target high-quality posterior.

Based on this insight, AdaDS operates in two stages. The first stage performs coarse refinement to produce an initial depth estimate and a variance map that quantifies uncertainty in the refinement. This uncertainty is then used to dynamically select a timestep that ensures both distributional similarity and input content preservation. In the second stage, a dedicated noise sampling module predicts timestep-conditioned noise that, when added to the coarse estimate, yields an intermediate latent aligned with the high-density manifold of the high-quality depth distribution. This carefully positioned noisy sample is denoised by the pre-trained diffusion model to recover the final high-resolution depth map. By design, even imperfections in the upstream refinement are tolerated, as adequate noising projects the sample onto the learned generative prior, conferring inherent robustness to diverse degradations.

The main contributions of this work are three-fold:

- We introduce AdaDS, a highly generalizable frame-

work that effectively addresses the long-standing robustness challenge in DSR, enabling accurate reconstruction across arbitrary upsampling factors, diverse degradation patterns, and unseen real-world scenes.

- We propose a novel adaptive sampling strategy that exploits the convergence property of forward diffusion processes to dynamically align an intermediate noisy sample with the high-probability region of the target high-quality depth posterior, thereby leveraging the powerful generative prior of a pre-trained diffusion model to achieve inherent robustness.
- We conduct extensive experiments on both real-world and synthetic benchmarks, demonstrating AdaDS’s superior zero-shot generalization and resilience compared to state-of-the-art approaches.

## 2. Related Work

**Depth Super-Resolution.** Early DSR works mainly operated under synthetic degradation scenarios, where low-resolution inputs were generated by downsampling ground-truth depth maps. In this controlled setting, research primarily concentrated on restoring high-frequency details lost during downsampling (Guo et al., 2018; Zhao et al., 2022; Yuan et al., 2023b). The subsequent availability of real-world datasets (He et al., 2021; Yan et al., 2024a) introduced more practical and diverse degradation patterns, highlighting the limitations of prior approaches. Recent methods have sought to address these challenges through specialized techniques. For instance, SFG (Yuan et al., 2023a) employs structure flow guidance to transfer structural information from RGB images; IDSR (Yan et al., 2024b) incorporates an auxiliary depth completion branch to handle invalid measurements; DORNet (Wang et al., 2025c) learns degradation-aware representations in a self-supervised manner to enhance cross-modal feature fusion; and SDCL (Ye et al., 2025) introduces semantic-driven contrastive learning to align depth edges with semantic contours. Despite achieving impressive performance on in-domain benchmarks, these approaches often exhibit limited generalization to out-of-distribution degradations and unseen real-world scenarios, constraining their practical deployment.

**Depth Diffusion Models.** Diffusion models have recently emerged as a powerful approach for high-fidelity depth estimation. Marigold (Ke et al., 2024) pioneered this direction by fine-tuning a Stable Diffusion model on limited synthetic data, enabling strong zero-shot performance with fine-grained outputs. Subsequent works have advanced the paradigm. For example, GeoWizard (Fu et al., 2024) facilitates mutual information exchange between depth and surface normals for enhanced geometric consistency; Lotus (He et al., 2024) mitigates undesirable variance in the generative process by directly predicting deterministic an-

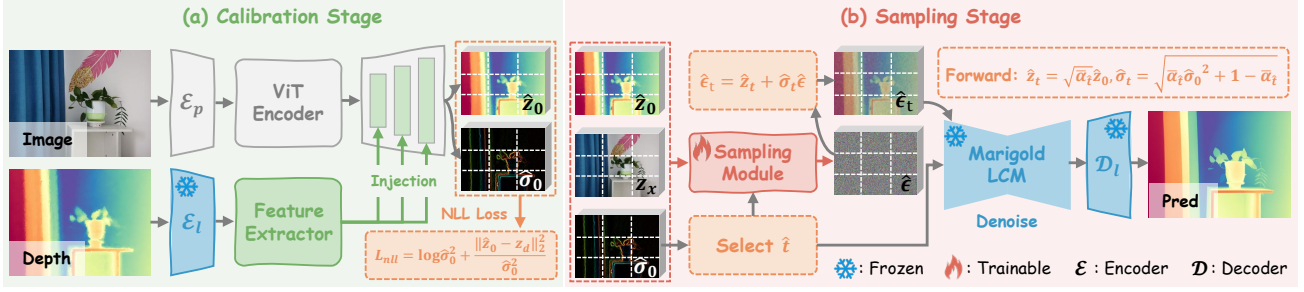


**Figure 3. Overall framework of AdaDS.** (a) The first stage produces a refined depth latent along with an estimated uncertainty map reflecting refinement reliability. (b) The second stage blends the coarse refinement with estimated noise, aligning it with the high-probability region of the target high-quality depth posterior. The produced noise is denoised to recover the final depth map via a pre-trained depth diffusion model.  $\mathcal{E}_p$ ,  $\mathcal{E}_l$  and  $\mathcal{D}_l$  denote the patch embedding, latent encoder and latent decoder, respectively.

notations; DepthFM (Gui et al., 2025) significantly accelerates sampling through flow matching techniques; and Jasmine (Wang et al., 2025a) extends the diffusion framework to self-supervised learning settings. Furthermore, hybrid approaches such as BetterDepth (Zhang et al., 2024) and SharpDepth (Pham et al., 2025) have sought to combine the strong generalization of large-scale discriminative pre-training with the superior detail recovery of diffusion-based generative modeling, striking an effective balance between accuracy and visual sharpness. Unlike these methods, AdaDS explicitly conditions the diffusion process on a low-resolution depth input. By adaptively perturbing this input with learned, timestep-aligned noise, AdaDS leverages the pre-trained diffusion prior to perform robust denoising.

### 3. Depth Diffusion Model Preliminary

Our framework employs the pre-trained Marigold-LCM (Ke et al., 2024) as the denoiser, benefiting from its strong modeling of high-quality depth distributions and efficient one-step inference capability. It is obtained by distilling a Denoising Diffusion Probabilistic Model (DDPM) (Ho et al., 2020) based teacher model using the Latent Consistency Model (LCM) (Song et al., 2023), preserving the same marginal forward distributions as the original DDPM.

Specifically, given an RGB image  $\mathbf{x}$  and its corresponding depth map  $\mathbf{d}$ , both are first encoded into the latent space  $\mathbf{z}_x = \mathcal{E}_l(\mathbf{x})$  and  $\mathbf{z}_d = \mathcal{E}_l(\mathbf{d})$  via a frozen VAE (Kingma & Welling, 2014) encoder  $\mathcal{E}_l(\cdot)$ . In the forward diffusion process, the depth latent  $\mathbf{z}_d$  is progressively corrupted by Gaussian noise according to the conditional distribution:

$$p(\mathbf{z}_t \mid \mathbf{z}_d, \mathbf{z}_x) = \mathcal{N}(\sqrt{\bar{\alpha}_t} \mathbf{z}_d, (1 - \bar{\alpha}_t) \mathbf{I}), \quad (1)$$

where  $\bar{\alpha}_t = \prod_{s=1}^t (1 - \beta_s) \in [0, 1]$  is the cumulative product of the noise schedule (with  $\beta_s$  increasing over timesteps  $t$ ), and as  $t \rightarrow T$ ,  $\mathbf{z}_t$  converges to standard Gaussian noise. During inference, Marigold-LCM enables fast generation by directly predicting a denoised latent from an initial noisy sample. A standard Gaussian noise  $\epsilon \sim \mathcal{N}(\mathbf{0}, \mathbf{I})$  is sampled,

concatenated with  $\mathbf{z}_x$ , and passed to the model:

$$\hat{\mathbf{z}} = \text{LCM}(\mathbf{z}_x \parallel \epsilon), \quad (2)$$

where  $\parallel$  denotes channel-wise concatenation. The final depth map is then recovered as  $\hat{\mathbf{d}} = \mathcal{D}_l(\hat{\mathbf{z}})$  via the pre-trained VAE decoder  $\mathcal{D}_l(\cdot)$ .

### 4. AdaDS Framework

AdaDS is motivated by the contraction property inherent in Gaussian smoothing within the forward diffusion process. Let  $\mathbf{d}_{in}$  denote the degraded low-resolution (LR) depth input and  $\mathbf{z}_{in} = \mathcal{E}_l(\mathbf{d}_{in})$  its latent representation. As shown in Eq. (1), the distributional discrepancy between  $p(\mathbf{z}_t \mid \mathbf{z}_d, \mathbf{z}_x)$  and  $p(\mathbf{z}_t^{in} \mid \mathbf{z}_{in}, \mathbf{z}_x)$  progressively diminishes as  $\bar{\alpha}_t$  approaches 0. Simultaneously, the influence of the input content  $\mathbf{z}_{in}$  is increasingly erased. This convergence property implies the existence of an optimal trade-off timestep that balances fidelity to the input content with sufficient alignment to the target high-quality depth posterior. Building on this insight, AdaDS strategically perturbs a refined depth latent with timestep-dependent noise at the selected timestep, projecting the resulting noisy sample into the high-density region of the high-quality depth manifold learned by a pre-trained diffusion model. The model’s robust denoising capability then recovers a high-fidelity depth map from this carefully positioned intermediate. To implement this principle, we design AdaDS as a two-stage pipeline, as illustrated in Fig. 3.

**Calibration Stage.** The calibration stage is illustrated in Fig. 3 (a). It performs initial refinement on LR depth with two primary objectives: (1) Reducing the gap between the LR input and its high-quality counterpart, thereby avoiding excessively large timesteps that would erase important input content; (2) Estimating the predictive uncertainty (in the form of variance) of the refinement, which serves as the basis for adaptive timestep selection in the second stage.

To achieve these goals, we design a two-branch module

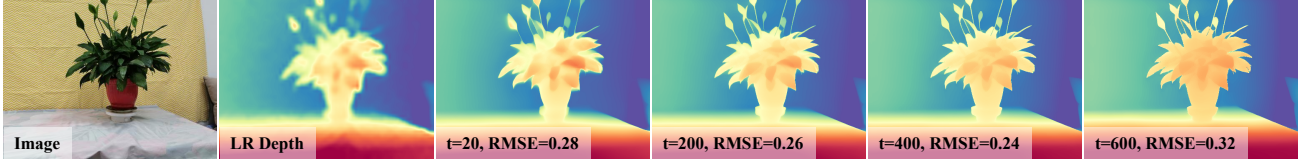


Figure 4. As  $t$  increases, the reconstructed depth maps exhibit enhanced fidelity and sharper structural details. However, this is accompanied by an increased deviation from the input depth measurements. All depth maps are visualized using a unified color palette, with RMSE metric reported in centimeters.

$\mathcal{R}(\cdot)$  that takes the image  $\mathbf{x}$  and interpolated  $\mathbf{d}_{in}$  as inputs, producing a refined depth latent and its associated uncertainty:  $(\hat{\mathbf{z}}_0, \hat{\sigma}_0) = \mathcal{R}(\mathbf{x}, \mathbf{d}_{in})$ , where  $\hat{\mathbf{z}}_0$  is the refined depth latent and  $\hat{\sigma}_0$  denotes the predicted standard deviation at each spatial location. The image branch fine-tunes a variant of Depth Anything V2 (Yang et al., 2024) to exploit its strong spatial perception capability. It consists of a patch embedding layer  $\mathcal{E}_p(\cdot)$  that downsamples the input image  $\mathbf{x}$  by a factor of 16, followed by a sequence of ViT (Dosovitskiy et al., 2021) blocks for global feature extraction, and a DPT (Ranftl et al., 2021) head for progressive feature up-sampling. The depth branch first encodes  $\mathbf{d}_{in}$  into the latent space  $\mathbf{z}_{in} = \mathcal{E}_l(\mathbf{d}_{in})$  at 1/8 scale. A UNet-like architecture (Ronneberger et al., 2015) then extracts multi-scale features at 1/32, 1/16, and 1/8 scales, which are injected into the DPT head of the image branch via element-wise addition to enhance depth-aware guidance. Training is supervised using two complementary losses. First, we adopt the Negative Log-Likelihood (NLL) loss (Kendall & Gal, 2017) to encourage well-calibrated uncertainty estimation:

$$\mathcal{L}_{nll} = \log \hat{\sigma}_0^2 + \frac{\|\hat{\mathbf{z}}_0 - \mathbf{z}_d\|_2^2}{\hat{\sigma}_0^2}, \quad (3)$$

where  $\mathbf{z}_d = \mathcal{E}_l(\mathbf{d})$  is the ground-truth depth latent. Second, to compensate for potential reconstruction errors introduced by the VAE encoder/decoder pair, we add an  $\ell_1$  supervision on the decoded depth map:

$$\mathcal{L}_d = \|\mathcal{D}_l(\hat{\mathbf{z}}_0) - \mathbf{d}\|_1. \quad (4)$$

**Sampling Stage.** As shown in Fig. 3(b), the second stage builds upon the outputs of the calibration stage to define an approximate forward diffusion process centered on the refined latent:

$$p(\hat{\mathbf{z}}_t \mid \hat{\mathbf{z}}_0, \hat{\sigma}_0, \mathbf{z}_x) = \mathcal{N}(\sqrt{\bar{\alpha}_t} \hat{\mathbf{z}}_0, (\bar{\alpha}_t \hat{\sigma}_0^2 + 1 - \bar{\alpha}_t) \mathbf{I}). \quad (5)$$

Before detailing the sampling procedure, we first introduce and prove a *proposition* that underpins our adaptive timestep selection strategy. Let  $\mathcal{W}(\cdot, \cdot)$  denote the 2-Wasserstein distance,  $\hat{p}_t$  the approximate forward distribution in Eq. (5), and  $p_t$  the ground-truth forward distribution in Eq. (1). We define the following objective function that trades off distributional alignment and content preservation:

$$\mathcal{H}(\bar{\alpha}_t) = \sqrt{\bar{\alpha}_t} \cdot \exp(-\lambda \mathcal{W}(\hat{p}_t, p_t)), \quad (6)$$

where  $\lambda > 0$  is a hyperparameter that controls the relative importance of the two terms.

**Proposition 4.1.** For  $\bar{\alpha}_t \in (0, 1]$ , the function  $\mathcal{H}(\bar{\alpha}_t)$  admits a unique global maximum.

*Proof.* For isotropic Gaussian distributions with same dimension, the 2-Wasserstein distance is exactly

$$\mathcal{W}(\hat{p}_t, p_t) = \sqrt{\bar{\alpha}_t (\|\hat{\mathbf{z}}_0 - \mathbf{z}_d\|_2^2 + \hat{\sigma}_0^2)}. \quad (7)$$

Here, we set  $\omega = \sqrt{\|\hat{\mathbf{z}}_0 - \mathbf{z}_d\|_2^2 + \hat{\sigma}_0^2}$  and omit the subscript for simplicity. Substituting above formulation gives

$$\mathcal{H}(\bar{\alpha}_t) = \sqrt{\bar{\alpha}_t} \cdot \exp(-\lambda \omega \sqrt{\bar{\alpha}_t}). \quad (8)$$

The derivative of  $\mathcal{H}(\bar{\alpha}_t)$  is

$$\frac{d\mathcal{H}}{d\bar{\alpha}_t} = \frac{\exp(-\lambda \omega \sqrt{\bar{\alpha}_t})}{2\sqrt{\bar{\alpha}_t}} (1 - \lambda \omega \sqrt{\bar{\alpha}_t}). \quad (9)$$

Setting the derivative to zero yields the critical point

$$\bar{\alpha}_t^* = \frac{1}{(\lambda \omega)^2}. \quad (10)$$

For  $\bar{\alpha}_t < \bar{\alpha}_t^*$ , the derivative is positive; for  $\bar{\alpha}_t > \bar{\alpha}_t^*$ , it is negative. Hence  $\mathcal{H}(\bar{\alpha}_t)$  has a unique global maximum.  $\square$

This proposition confirms the existence of an optimal  $\bar{\alpha}_t$  (and thus an optimal timestep  $t$ ) that best balances input fidelity and alignment to the target distribution. We further illustrate this in Fig. 4. During inference, since the ground-truth  $\mathbf{z}_d$  is unavailable, we approximate  $\omega$  using only the predicted uncertainty:

$$\omega \approx \bar{\sigma}_0 = \frac{1}{N} \sum_{i=1}^N \hat{\sigma}_0^{(i)}, \quad (11)$$

where  $\bar{\sigma}_0$  is the spatial average of the predicted standard deviations. We then select the smallest timestep  $\hat{t}$  such that  $\sqrt{\bar{\alpha}_{\hat{t}}} \bar{\sigma}_0 \leq \tau$  (or equivalently  $\bar{\alpha}_{\hat{t}} \leq (\tau/\bar{\sigma}_0)^2$ ). To avoid overly aggressive decay of  $\bar{\alpha}_{\hat{t}}$ , we adopt a simplified rule:

$$\bar{\alpha}_{\hat{t}} = \frac{\tau}{\bar{\sigma}_0}, \quad (12)$$

which is subsequently clamped to the valid interval

Table 1. Quantitative zero-shot comparison on real-world benchmarks. Input resolutions for the low-resolution depth maps are provided in the second row. For each metric, the best and second-best results are highlighted in **bold** and underline, respectively.

Method	Ref.	RGB-D-D						TOFDSR					
		192 × 144		64 × 48		32 × 24		192 × 144		64 × 48		32 × 24	
		RMSE ↓	MAE ↓										
DA v2-L	NeurIPS-24	0.1082	0.0745	0.1082	0.0745	0.1082	0.0745	0.1035	0.0690	0.1035	0.0690	0.1035	0.0690
MG-LCM	CVPR-24	0.1306	0.1007	0.1306	0.1007	0.1306	0.1007	0.1219	0.0835	0.1219	0.0835	0.1219	0.0835
SGNet	AAAI-24	0.0726	0.0388	0.0723	0.0391	0.0740	0.0416	0.0726	0.0400	0.0726	0.0404	0.0767	0.0433
C2PD	AAAI-25	0.0724	0.0388	0.0717	0.0384	0.0714	0.0384	<u>0.0723</u>	0.0403	<u>0.0718</u>	0.0400	<u>0.0722</u>	0.0405
DuCos	ICCV-25	0.0744	0.0388	0.0741	0.0385	0.0898	0.0555	<u>0.0742</u>	<u>0.0399</u>	0.0742	0.0399	0.0958	0.0594
PromptDA	CVPR-25	0.0706	0.0506	0.0705	0.0505	0.0704	0.0503	0.0879	0.0623	0.0885	0.0624	0.0884	0.0620
OMNI-DC	ICCV-25	0.0680	<u>0.0371</u>	0.0687	0.0385	0.0846	0.0468	0.0748	<u>0.0399</u>	0.0890	0.0451	0.1071	0.0535
MG-DC	ICCV-25	0.0685	0.0382	0.0684	0.0392	0.0826	0.0475	0.0780	0.0416	0.0844	0.0441	0.0980	0.0508
PriorDA	arXiv-25	<u>0.0655</u>	0.0379	<u>0.0613</u>	<u>0.0377</u>	<u>0.0691</u>	<u>0.0432</u>	0.0731	0.0411	0.0755	0.0435	0.0833	0.0480
<b>Our</b>	—	<b>0.0607</b>	<b>0.0332</b>	<b>0.0597</b>	<b>0.0330</b>	<b>0.0597</b>	<b>0.0342</b>	<b>0.0693</b>	<b>0.0336</b>	<b>0.0688</b>	<b>0.0346</b>	<b>0.0700</b>	<b>0.0363</b>

$[\bar{\alpha}_{min}, 1]$  to ensure  $\bar{\alpha}_t \in (0, 1]$ . Given  $\hat{t}$ , a lightweight noise sampling network  $\mathcal{S}(\cdot)$  takes as input the RGB latent  $\mathbf{z}_x$ , the predicted mean scale  $\hat{\mathbf{z}}_t = \sqrt{\bar{\alpha}_t} \hat{\mathbf{z}}_0$ , and the predicted noise scale  $\hat{\sigma}_t = \sqrt{\bar{\alpha}_t \hat{\sigma}_0^2 + 1 - \bar{\alpha}_t}$ , and outputs a noise prediction  $\hat{\epsilon} = \mathcal{S}(\mathbf{z}_x, \hat{\mathbf{z}}_t, \hat{\sigma}_t)$ . The intermediate noisy latent is formulated as

$$\hat{\epsilon}_t = \hat{\mathbf{z}}_t + \hat{\sigma}_t \hat{\epsilon}. \quad (13)$$

Finally,  $\hat{\epsilon}_t$  is fed into the pre-trained Marigold-LCM model for one-step denoising, yielding the refined depth latent  $\hat{\mathbf{z}}_d$ , which is decoded to the final high-resolution depth map  $\hat{\mathbf{d}} = \mathcal{D}_l(\hat{\mathbf{z}}_d)$ . To train the noise sampling network  $\mathcal{S}(\cdot)$ , we employ a reconstruction loss that encourages accurate recovery of both the latent and pixel-space depth:

$$\mathcal{L}_{rec} = \|\hat{\mathbf{z}}_d - \mathbf{z}_d\|_2^2 + \|\hat{\mathbf{d}} - \mathbf{d}\|_1. \quad (14)$$

Additionally, we incorporate a gradient loss to encourage spatial smoothness and edge preservation in the predicted depth map:

$$\mathcal{L}_g = \|\partial_x \hat{\mathbf{d}} - \partial_x \mathbf{d}\|_1 + \|\partial_y \hat{\mathbf{d}} - \partial_y \mathbf{d}\|_1, \quad (15)$$

where  $\partial_x$  and  $\partial_y$  denote the horizontal and vertical spatial gradients, respectively.

#### 4.1. Implementation Details

**Dataset Details.** We train AdaDS on the **Hypersim** dataset (Roberts et al., 2021), which provides high-quality synthetic RGB-depth pairs collected under realistic indoor conditions. To ensure stability, we filter out samples containing large invalid depth regions, resulting in a final training set of around 56K samples. For each sample, the ground-truth depth map is downsampled using random scaling factors to generate the LR input. To mimic real-world sensor degradations, we further apply a series of augmentations to the LR depth maps, including Gaussian noise, random filtering and sparse

point removal. For the sparsity simulation, we randomly discard pixels and fill the missing regions using a KNN-based inpainting approach, approximating the sparse and irregular measurements typical of real-world range sensors.

**Network Details.** The calibration stage employs the ViT-Small variant of Depth Anything V2 as its image backbone for strong spatial perception. We further adapt the window size of its patch embedding layer to 16 for compatible feature size with LR input. Both feature extractor and noise sampling module use lightweight UNet-like architecture built from ConvNeXt (Liu et al., 2022) blocks and transposed convolutions. Overall, AdaDS contains approximately 40.3M trainable parameters.

**Training Details.** We train the two stages of AdaDS independently. The calibration stage is trained for 42K iterations, and the sampling stage for 35K iterations, both with a batch size of 8. Training is performed on 4 NVIDIA RTX 4090 GPUs and takes approximately 14 hours in total. We adopt the OneCycle learning rate policy (Smith & Topin, 2019) with an initial learning rate of  $10^{-5}$ , which progressively increases to a peak of  $10^{-4}$  over the first 10% of iterations and then decays to  $10^{-5}$  following a cosine schedule. The training objectives for the first and second stages are defined as  $\mathcal{L}_1 = \mathcal{L}_{nll} + \beta \mathcal{L}_d$  and  $\mathcal{L}_2 = \mathcal{L}_{rec} + \mathcal{L}_g$ , respectively. The balancing hyperparameters are set to  $\beta = 0.5$ .

## 5. Experiment

### 5.1. Experiment Setup

To assess the zero-shot generalization and robustness of AdaDS, we evaluate on both real-world and synthetic benchmarks. For *real-world* evaluation, we use two datasets: **RGB-D-D** (He et al., 2021) and **TOFDSR** (Yan et al., 2024a). Both contain LR depth maps captured by a mobile ToF camera at  $192 \times 144$  resolution, paired with high-

Table 2. Quantitative zero-shot comparison on synthetic benchmarks. DS., GN., GB., SM. and LC. denote downsampling, Gaussian noise, Gaussian blur, sparse measurement and low-bit compression, respectively. RMSE metric is reported in this table.

Method	Ref.	ScanNet					NYUv2				
		16× DS.	DS. + GN.	DS. + GB.	DS. + SM.	DS. + LC.	16× DS.	DS. + GN.	DS. + GB.	DS. + SM.	DS. + LC.
DA v2-L	NeurIPS-24	0.1416	0.1416	0.1416	0.1416	0.1416	0.2075	0.2075	0.2075	0.2075	0.2075
MG-LCM	CVPR-24	0.1986	0.1986	0.1986	0.1986	0.1986	0.2587	0.2587	0.2587	0.2587	0.2587
PromptDA	CVPR-25	0.0927	0.0983	0.0935	0.0953	0.0950	0.1326	0.1352	0.1349	0.1369	0.1338
OMNI-DC	ICCV-25	0.1173	0.1224	0.1127	0.1188	0.1206	0.1966	0.2011	0.1894	0.2003	0.1980
MG-DC	ICCV-25	0.1222	0.1288	0.1173	0.1214	0.1262	0.2027	0.2077	0.1951	0.2025	0.2052
PriorDA	arXiv-25	0.0933	0.0949	0.0953	0.0954	0.0944	0.1432	0.1444	0.1474	0.1458	0.1439
<b>Our</b>	—	<b>0.0754</b>	<b>0.0783</b>	<b>0.0810</b>	<b>0.0834</b>	<b>0.0773</b>	<b>0.1197</b>	<b>0.1217</b>	<b>0.1289</b>	<b>0.1315</b>	<b>0.1206</b>

precision ground-truth depth maps acquired by a high-end ToF sensor at  $512 \times 384$  resolution. During testing, we apply bicubic downsampling to the original LR inputs to simulate varying upsampling factors. For *synthetic* evaluation, we adopt **NYUv2** (Silberman et al., 2012) and **ScanNet** (Dai et al., 2017), which provide high-quality RGB-depth pairs from indoor scenes. To simulate realistic degradations, we synthesize LR inputs by first applying bicubic downsampling to the ground-truth depth maps, followed by a combination of common real-world artifacts, including additive Gaussian noise, Gaussian blur, pixel removal, and low-bit compression. Invalid pixels in the ground-truth depth maps are filled using a colorization-based inpainting method (Levin et al., 2004) prior to degradation simulation. All quantitative metrics are computed exclusively on valid ground-truth pixels to prevent bias from missing depth values. We report three standard depth estimation metrics, including Root Mean Squared Error (RMSE) and Mean Absolute Error (MAE) for absolute accuracy, and threshold accuracy  $\delta_{1.05}$  for relative precision. Please refer to the appendix for more details.

## 5.2. Comparison with the State-of-the-Art

We compare AdaDS against a range of state-of-the-art (SOTA) methods, including Depth Anything V2 (DA v2) (Yang et al., 2024), Marigold-LCM (MG-LCM) (Ke et al., 2024), SGNet (Wang et al., 2024c), C2PD (Kang et al., 2025), DuCos (Yan et al., 2025a), PromptDA (Lin et al., 2025), OMNI-DC (Zuo et al., 2025), Marigold-DC (MG-DC) (Viola et al., 2025) and PriorDA (Wang et al., 2025b).

**Real-World Evaluation.** Quantitative results on the real-world benchmarks are reported in Tab. 1. AdaDS consistently achieves substantial improvements over all competing methods across every metric and upsampling factor, demonstrating its superior performance and robustness on real-world DSR tasks. For instance, on the original input resolution of the RGB-D-D dataset, AdaDS outperforms the second-best method, PriorDA by 7.33% in RMSE. On the TOFDSR dataset, it surpasses C2PD by 4.15% in RMSE

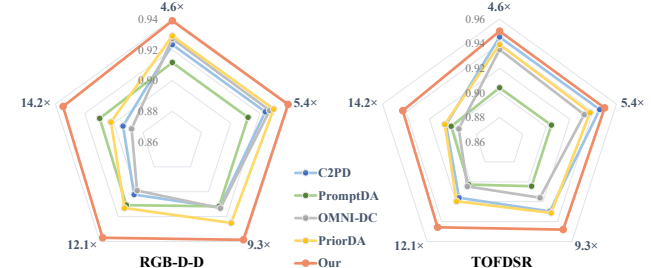


Figure 5. Comparison on real-world benchmarks with arbitrary upsampling factors. The  $\delta_{1.05} \uparrow$  metric is reported in this figure.

metric. Notably, AdaDS exhibits remarkable stability with respect to input resolution changes, maintaining nearly consistent performance across all tested upsampling factors. In contrast, competing methods show clear brittleness. For example, the RMSE of MG-DC deteriorates by 20.58% when the upsampling factor increases from  $2.7\times$  to  $16\times$ . We further evaluate generalization to arbitrary (non-integer) upsampling factors and present the results in Fig. 5.

**Synthetic Evaluation.** The quantitative results on synthetic benchmarks are summarized in Tab. 2. To rigorously assess robustness under severe degradations, we downsample the ground-truth depth maps by a factor of 16 and apply a diverse set of realistic degradation patterns, including Gaussian noise, Gaussian blur, random sparsity, and low-bit compression, mimicking common real-world sensor imperfections. Across all degradation types and both datasets, AdaDS significantly outperforms all baseline methods. On average, it improves over the second-best approach, PromptDA, by 16.91% on ScanNet and 7.57% on NYUv2, highlighting its strong generalization and resilience to complex, compound degradations.

**Qualitative Comparison.** Qualitative results on real-world benchmarks are presented in Fig. 6. AdaDS produces depth maps with substantially lower overall prediction error (as visualized in the error maps) while recovering fine-grained geometric details and sharp boundaries in the highlighted regions, outperforming all competitors. On synthetic benchmarks reported in Fig. 7, we back-project the predicted

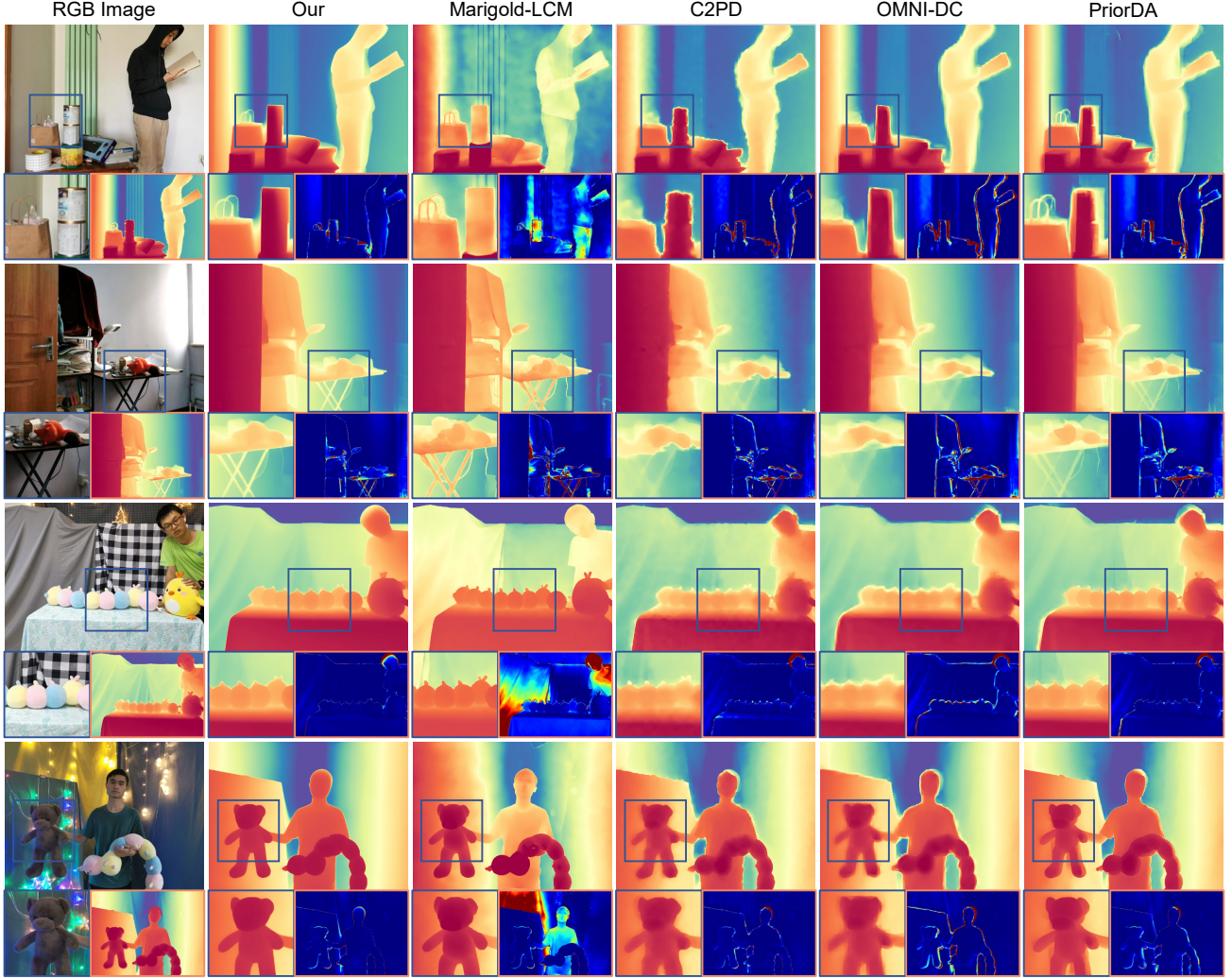


Figure 6. Qualitative comparison on real-world benchmarks. The first two rows present samples from the RGB-D-D dataset, while the subsequent two rows showcase examples from TOFDSR. Corresponding error maps are provided in the bottom-right inset of each result, where warmer colors (red) denote higher prediction error.

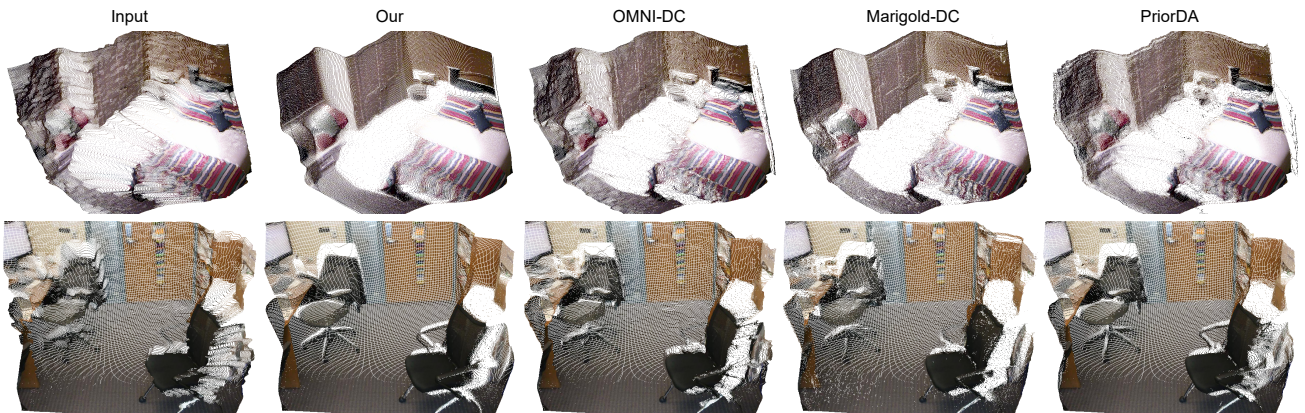


Figure 7. Qualitative comparison on synthetic benchmarks. The first and second rows display samples from the NYUv2 and ScanNet datasets, respectively. To facilitate 3D structural evaluation, the estimated depth maps are back-projected into 3D point clouds and colorized using their corresponding RGB images.

Table 3. Ablation study on real-world benchmarks at  $8\times$  factor.

	RGB-D-D		TOFDSR	
	RMSE $\downarrow$	MAE $\downarrow$	RMSE $\downarrow$	MAE $\downarrow$
(a) DA v2-S Baseline	0.1265	0.0900	0.1252	0.0740
(b) Our Calibration Stage	0.0627	0.0358	0.0694	0.0379
(c) (b) + Directly Regressing $\hat{z}$	0.0613	0.0346	0.0710	0.0379
(d) (c) + MG-LCM Denoising	0.0622	0.0367	0.0723	0.0391
(e) Replace $\hat{t}$ with Random $t$	0.0768	0.0497	0.0809	0.0455
(f) Replace $\hat{e}$ with Gaussian Noise	0.0668	0.0387	0.0742	0.0394
<b>Our</b>	<b>0.0597</b>	<b>0.0330</b>	<b>0.0688</b>	<b>0.0346</b>

depth maps into 3D point clouds to better illustrate structural fidelity. Our method effectively restores severely distorted structures from heavily degraded inputs, preserving both local details and global scene geometry with noticeably higher quality than existing approaches.

## 6. Ablation Study

We perform comprehensive ablation studies on real-world benchmarks, with quantitative results reported in Tab. 3. Our calibration stage (b) is built on DA v2-Small backbone (a) and designed to effectively fuse LR depth information with RGB guidance. It delivers substantial gains over (a), reducing RMSE by 50.43% on RGB-D-D and 44.57% on TOFDSR. This confirms the critical rule of incorporating LR depth cues. To highlight the superiority of our diffusion sampling strategy over direct regression, we introduce variant (c), which replaces the noise sampling and diffusion operations with direct regression of the final depth latent  $\hat{z}$ . It performs substantially worse than the full AdaDS model, with RMSE increases of 2.68% on RGB-D-D and 3.20% on TOFDSR. Notably, on TOFDSR it underperforms even the first stage (b), underscoring that direct regression is particularly fragile in zero-shot settings with limited training data. Variant (d) projects the predicted latent from (c) into the forward diffusion process at the same timestep as our full model and applies MG-LCM denoising without any learned noise adaptation. The results are inferior to those of (c), confirming that the pre-trained diffusion model requires carefully tailored noisy intermediates rather than naive forward projection. When our timestep selection rule (Eq. (12)) is replaced with uniformly random timesteps (e), performance drops sharply, validating the importance of the adaptive rule in balancing input content preservation and distributional alignment. Similarly, substituting the learned noise prediction  $\hat{e}$  from the sampling module with standard Gaussian noise (f) results in substantial degradation, demonstrating the effectiveness of the dedicated noise sampling module  $\mathcal{S}(\cdot)$  in positioning the intermediate latent within the high-probability region of the target posterior.

We further investigate the sensitivity to the threshold  $\tau$  in the

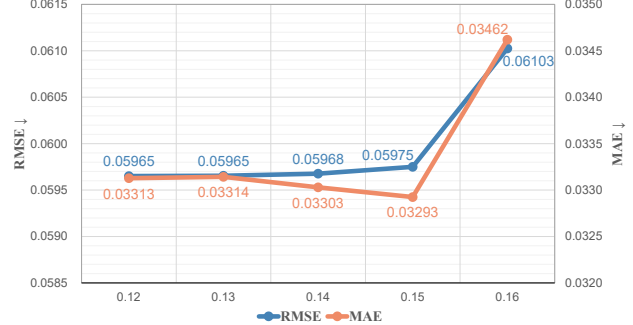


Figure 8. Parameter validation experiment on timestep selection parameter  $\tau$ . The x axis indicates the  $\tau$  values. All models are separately trained using the indicated  $\tau$ .

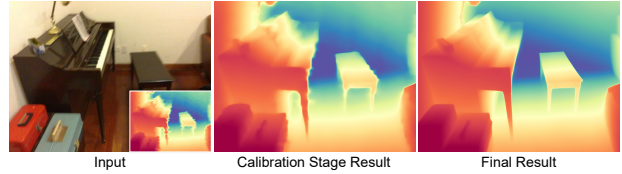


Figure 9. Visual comparison between the intermediate result from the calibration stage and the final depth prediction.

timestep selection rule. Results are shown in Fig. 8. AdaDS remains robust for small values of  $\tau$ , but performance deteriorates significantly at  $\tau = 0.16$ . Larger  $\tau$  selects very small timesteps that preserve input content but severely limit the model’s ability to correct upstream errors. We adopt  $\tau = 0.14$  in all experiments, as it provides the best trade-off between RMSE and MAE.

Finally, Fig. 9 visually compares the intermediate output of the calibration stage with the final prediction. When the input depth is heavily degraded, the calibration stage recovers a large portion of the structural content and substantially narrows the distributional gap to high-quality depth, although residual inaccuracies remain. Based on this intermediate estimate, our adaptive noise sampling and diffusion denoising effectively correct these imperfections, producing a high-fidelity final depth map.

## 7. Conclusion

Generalization and robustness remain persistent challenges in DSR tasks, particularly under diverse real-world degradations and unseen scenarios. We address this by exploiting the contraction property in diffusion models, where degraded inputs progressively align with high-quality depth distributions. Building on this insight, we propose AdaDS, a two-stage framework that performs uncertainty-aware calibration followed by adaptive noise injection to position intermediates in the high-probability region of the target posterior learned by a pre-trained diffusion model. Extensive experiments demonstrate AdaDS’s superior zero-shot robustness to arbitrary upsampling factors and degradations.

## Impact Statement

This paper presents work whose goal is to advance the field of Machine Learning. There are many potential societal consequences of our work, none which we feel must be specifically highlighted here.

## References

Chung, J., Oh, J., and Lee, K. M. Depth-regularized optimization for 3d gaussian splatting in few-shot images. In *CVPR*, pp. 811–820, 2024.

Dai, A., Chang, A. X., Savva, M., Halber, M., Funkhouser, T., and Nießner, M. ScanNet: Richly-Annotated 3D Reconstructions of Indoor Scenes. In *CVPR*, 2017.

Dong, X., Garratt, M. A., Anavatti, S. G., and Abbass, H. A. Towards real-time monocular depth estimation for robotics: A survey. *IEEE Transactions on Intelligent Transportation Systems*, pp. 16940–16961, 2022.

Dosovitskiy, A., Beyer, L., Kolesnikov, A., Weissenborn, D., Zhai, X., Unterthiner, T., Dehghani, M., Minderer, M., Heigold, G., Gelly, S., Uszkoreit, J., and Houlsby, N. An image is worth 16x16 words: Transformers for image recognition at scale. In *ICLR*, 2021.

Du, R., Turner, E., Dzitsiuk, M., Prasso, L., Duarte, I., Douragian, J., Afonso, J., Pascoal, J., Gladstone, J., Cruces, N., et al. Depthlab: Real-time 3d interaction with depth maps for mobile augmented reality. In *UIST*, pp. 829–843, 2020.

Fan, J., Wang, K., Yan, Z., Chen, X., Gao, S., Li, J., and Yang, J. Depth-centric dehazing and depth-estimation from real-world hazy driving video. In *AAAI*, pp. 2852–2860, 2025.

Fu, X., Yin, W., Hu, M., Wang, K., Ma, Y., Tan, P., Shen, S., Lin, D., and Long, X. Geowizard: Unleashing the diffusion priors for 3d geometry estimation from a single image. In *ECCV*, pp. 241–258, 2024.

Gui, M., Schusterbauer, J., Prestel, U., Ma, P., Kotovenko, D., Grebenkova, O., Baumann, S. A., Hu, V. T., and Ommer, B. Depthfm: Fast generative monocular depth estimation with flow matching. In *AAAI*, pp. 3203–3211, 2025.

Guo, C., Li, C., Guo, J., Cong, R., Fu, H., and Han, P. Hierarchical features driven residual learning for depth map super-resolution. *IEEE Transactions on Image Processing*, pp. 2545–2557, 2018.

He, J., Li, H., Yin, W., Liang, Y., Li, L., Zhou, K., Zhang, H., Liu, B., and Chen, Y.-C. Lotus: Diffusion-based visual foundation model for high-quality dense prediction. *arXiv preprint arXiv:2409.18124*, 2024.

He, L., Zhu, H., Li, F., Bai, H., Cong, R., Zhang, C., Lin, C., Liu, M., and Zhao, Y. Towards fast and accurate real-world depth super-resolution: Benchmark dataset and baseline. In *CVPR*, pp. 9229–9238, 2021.

Ho, J., Jain, A., and Abbeel, P. Denoising diffusion probabilistic models. *NeurIPS*, pp. 6840–6851, 2020.

Holynski, A. and Kopf, J. Fast depth densification for occlusion-aware augmented reality. *ACM Transactions on Graphics*, pp. 1–11, 2018.

Kang, J., Cai, Q., Tan, R., Liu, Y., and Liu, Z. C2pd: Continuity-constrained pixelwise deformation for guided depth super-resolution. In *AAAI*, pp. 4212–4220, 2025.

Ke, B., Obukhov, A., Huang, S., Metzger, N., Daudt, R. C., and Schindler, K. Repurposing diffusion-based image generators for monocular depth estimation. In *CVPR*, pp. 9492–9502, 2024.

Kendall, A. and Gal, Y. What uncertainties do we need in bayesian deep learning for computer vision? In *NeurIPS*, 2017.

Kingma, D. P. and Welling, M. Auto-encoding variational bayes. In *ICLR*, 2014.

Levin, A., Lischinski, D., and Weiss, Y. Colorization using optimization. *ACM Transactions on Graphics*, pp. 689–694, 2004.

Lin, H., Peng, S., Chen, J., Peng, S., Sun, J., Liu, M., Bao, H., Feng, J., Zhou, X., and Kang, B. Prompting depth anything for 4k resolution accurate metric depth estimation. In *CVPR*, pp. 17070–17080, 2025.

Liu, Z., Mao, H., Wu, C.-Y., Feichtenhofer, C., Darrell, T., and Xie, S. A convnet for the 2020s. In *CVPR*, pp. 11976–11986, 2022.

Pham, D.-H., Do, T., Nguyen, P., Hua, B.-S., Nguyen, K., and Nguyen, R. Sharpdepth: Sharpening metric depth predictions using diffusion distillation. In *CVPR*, pp. 17060–17069, 2025.

Ranftl, R., Bochkovskiy, A., and Koltun, V. Vision transformers for dense prediction. In *ICCV*, pp. 12179–12188, 2021.

Roberts, M., Ramapuram, J., Ranjan, A., Kumar, A., Bautista, M. A., Paczan, N., Webb, R., and Susskind, J. M. Hypersim: A photorealistic synthetic dataset for holistic indoor scene understanding. In *ICCV*, 2021.

Ronneberger, O., Fischer, P., and Brox, T. U-net: Convolutional networks for biomedical image segmentation. In *MICCAI*, pp. 234–241, 2015.

Sheng, H., Cai, S., Zhao, N., Deng, B., Zhao, M.-J., and Lee, G. H. Pdr: Progressive depth regularization for monocular 3d object detection. *IEEE Transactions on Circuits and Systems for Video Technology*, pp. 7591–7603, 2023.

Shi, W., Ye, M., and Du, B. Symmetric uncertainty-aware feature transmission for depth super-resolution. In *ACM MM*, pp. 3867–3876, 2022.

Silberman, N., Hoiem, D., Kohli, P., and Fergus, R. Indoor segmentation and support inference from rgbd images. In *ECCV*, pp. 746–760, 2012.

Smith, L. N. and Topin, N. Super-convergence: Very fast training of neural networks using large learning rates. In *Artificial intelligence and machine learning for multi-domain operations applications*, pp. 369–386, 2019.

Song, Y., Dhariwal, P., Chen, M., and Sutskever, I. Consistency models. In *ICML*, pp. 32211–32252, 2023.

Viola, M., Qu, K., Metzger, N., Ke, B., Becker, A., Schindler, K., and Obukhov, A. Marigold-dc: Zero-shot monocular depth completion with guided diffusion. In *ICCV*, pp. 5359–5370, 2025.

Wang, J., Lin, C., Guan, C., Nie, L., He, J., Li, H., Liao, K., and Zhao, Y. Jasmine: Harnessing diffusion prior for self-supervised depth estimation. *arXiv preprint arXiv:2503.15905*, 2025a.

Wang, K., Yan, Z., Fan, J., Zhu, W., Li, X., Li, J., and Yang, J. Dcdepth: Progressive monocular depth estimation in discrete cosine domain. *NeurIPS*, pp. 64629–64648, 2024a.

Wang, K., Yan, Z., Tian, H., Zhang, Z., Li, X., Li, J., and Yang, J. Altnerf: Learning robust neural radiance field via alternating depth-pose optimization. In *AAAI*, pp. 5508–5516, 2024b.

Wang, Z., Yan, Z., and Yang, J. Sgnet: Structure guided network via gradient-frequency awareness for depth map super-resolution. In *AAAI*, pp. 5823–5831, 2024c.

Wang, Z., Chen, S., Yang, L., Wang, J., Zhang, Z., Zhao, H., and Zhao, Z. Depth anything with any prior. *arXiv preprint arXiv:2505.10565*, 2025b.

Wang, Z., Yan, Z., Pan, J., Gao, G., Zhang, K., and Yang, J. Dornet: A degradation oriented and regularized network for blind depth super-resolution. In *CVPR*, pp. 15813–15822, 2025c.

Yan, Z., Lin, Y., Wang, K., Zheng, Y., Wang, Y., Zhang, Z., Li, J., and Yang, J. Tri-perspective view decomposition for geometry-aware depth completion. In *CVPR*, pp. 4874–4884, 2024a.

Yan, Z., Wang, K., Li, X., Zhang, Z., Li, G., Li, J., and Yang, J. Learning complementary correlations for depth super-resolution with incomplete data in real world. *IEEE Transactions on Neural Networks and Learning Systems*, pp. 5616–5626, 2024b.

Yan, Z., Wang, Z., Dong, H., Li, J., Yang, J., and Lee, G. H. Ducos: Duality constrained depth super-resolution via foundation model. In *ICCV*, 2025a.

Yan, Z., Wang, Z., Wang, K., Li, J., and Yang, J. Completion as enhancement: A degradation-aware selective image guided network for depth completion. In *CVPR*, pp. 26943–26953, 2025b.

Yang, L., Kang, B., Huang, Z., Zhao, Z., Xu, X., Feng, J., and Zhao, H. Depth anything v2. In *NeurIPS*, pp. 21875–21911, 2024.

Ye, X., Zhang, A., and Xu, R. Semantics-driven contrastive learning for real-world depth super resolution. In *ACM MM*, pp. 3085–3093, 2025.

Yuan, J., Jiang, H., Li, X., Qian, J., Li, J., and Yang, J. Structure flow-guided network for real depth super-resolution. In *AAAI*, pp. 3340–3348, 2023a.

Yuan, J., Jiang, H., Li, X., Qian, J., Li, J., and Yang, J. Recurrent structure attention guidance for depth super-resolution. In *AAAI*, pp. 3331–3339, 2023b.

Zhang, X., Ke, B., Riemenschneider, H., Metzger, N., Obukhov, A., Gross, M., Schindler, K., and Schroers, C. Betterdepth: Plug-and-play diffusion refiner for zero-shot monocular depth estimation. In *NeurIPS*, pp. 108674–108709, 2024.

Zhao, Z., Zhang, J., Xu, S., Lin, Z., and Pfister, H. Discrete cosine transform network for guided depth map super-resolution. In *CVPR*, pp. 5697–5707, 2022.

Zhong, Z., Liu, X., Jiang, J., Zhao, D., and Ji, X. Deep attentional guided image filtering. *IEEE Transactions on Neural Networks and Learning Systems*, pp. 12236–12250, 2023.

Zuo, Y., Yang, W., Ma, Z., and Deng, J. Omni-dc: Highly robust depth completion with multiresolution depth integration. In *ICCV*, pp. 9287–9297, 2025.

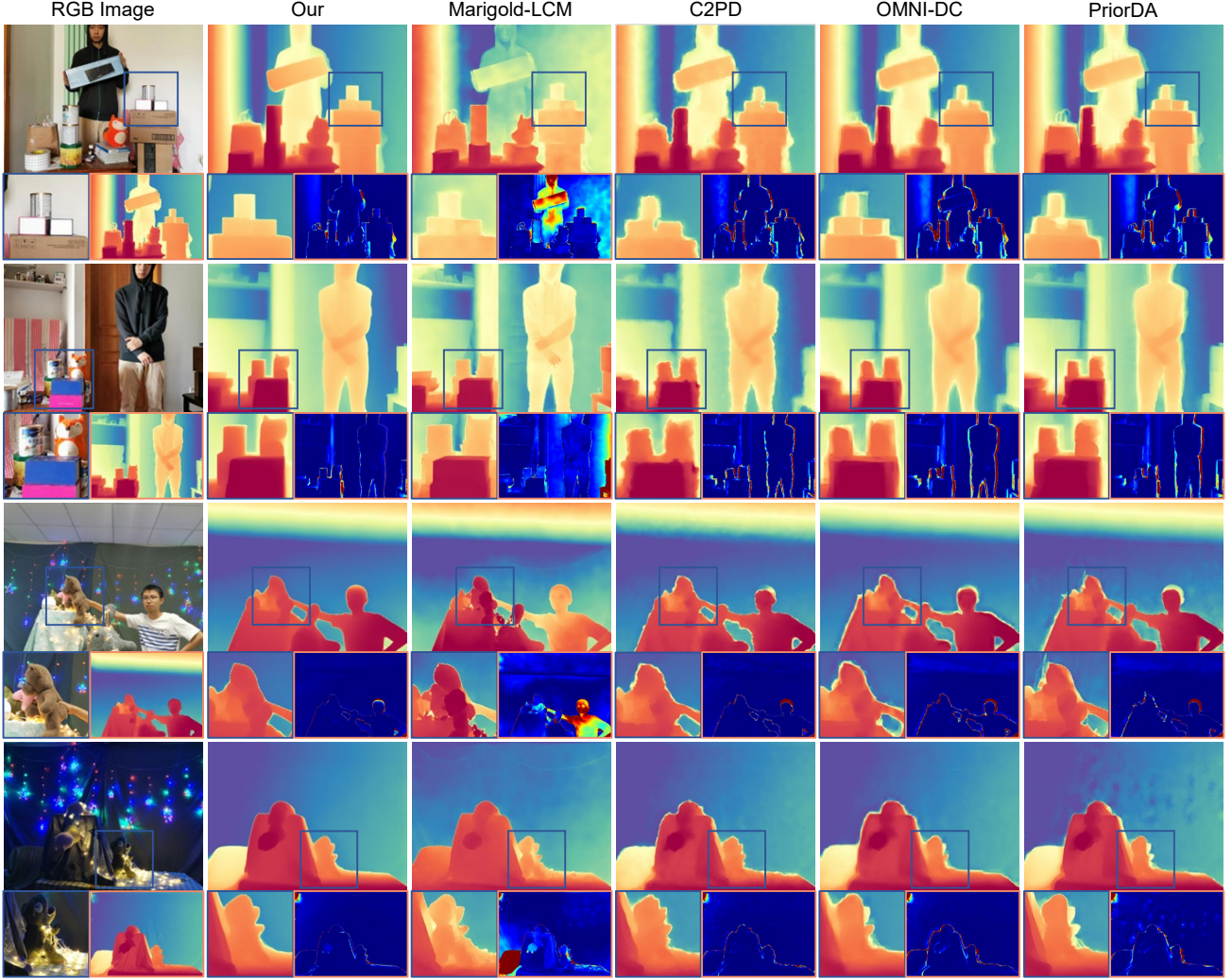


Figure 10. Qualitative comparison on real-world benchmarks. The first and last two samples are from RGB-D-D and TOFDSR datasets, respectively. The blue boxes highlight the regions where our method outperforms and the error maps are shown in the right bottom side.

## A. Additional Experimental Detail

For real-world evaluation, we follow the official data splits for the RGB-D-D (He et al., 2021) and TOFDSR (Yan et al., 2024a) datasets, which consist of 405 and 560 test samples, respectively. For the NYUv2 dataset, we utilize the standard split for monocular depth estimation, resulting in 654 test samples. Regarding ScanNet, since the official test split contains a vast number of video frames, we perform uniform sampling to select 500 frames for evaluation. Both synthetic datasets are processed at a resolution of . To address invalid depth measurements in the ground truth, we apply the same colorization-based inpainting approach (Levin et al., 2004) used in NYUv2 prior to synthesizing the LR depth maps.

To evaluate the performance under realistic degradations, we simulate common real-world degradation patterns within our synthetic benchmarks. First, the ground truth depth maps are downsampled to the target input resolution. Subsequently, we apply several perturbing operations:

- **Gaussian Noise:** Additive noise is sampled from  $\mathcal{N}(0, 0.05)$ .
- **Gaussian Blur:** Applied using a kernel size of 3 and a standard deviation of 0.5.
- **Pixel Removal:** To simulate the sparse measurements characteristic of range sensors, we randomly remove 30% of the pixels and fill the resulting gaps using the average value of the three nearest neighbors.



Figure 11. Qualitative comparison on NYUv2 dataset. The estimated depth map is back-projected to 3D point clouds to better demonstrate our superiority in the geometric accuracy.



Figure 12. Qualitative comparison on ScanNet dataset. The estimated depth map is back-projected to 3D point clouds to better demonstrate our superiority in the geometric accuracy.

- **Low-Bit Compression:** This is simulated by clipping the floating-point precision to decimeter levels.

We compare our method against a range of DSR and related methods. For methods originally designed for affine-invariant depth estimation (DA v2 and MG-LCM), we apply a Theil–Sen regression-based affine calibration to align their predictions with the ground truth scale before computing quantitative metrics. For depth completion-oriented approaches (OMNI-DC and MG-DC), we place the original LR depth values onto the corresponding upsampled grid positions and leave all other pixels empty, allowing the models to perform completion as intended in their formulations.

We employ three metrics to evaluate the depth prediction accuracy, including Root Mean Squared Error (RMSE) and Mean Absolute Error (MAE) for absolute accuracy, and threshold accuracy  $\delta_{1.05}$  for relative precision. Denote the predicted and ground truth depth map as  $\hat{\mathbf{d}}$  and  $\mathbf{d}$ , respectively, the above metrics are defined as follows:

$$\begin{aligned}
 \text{RMSE} &= \sqrt{\frac{1}{|\mathbf{d}|} \sum \|\hat{\mathbf{d}} - \mathbf{d}\|_2^2}, \\
 \text{MAE} &= \frac{1}{|\mathbf{d}|} \sum \|\hat{\mathbf{d}} - \mathbf{d}\|_1, \\
 \delta_{1.05} &= \max\left(\frac{\hat{\mathbf{d}}}{\mathbf{d}}, \frac{\mathbf{d}}{\hat{\mathbf{d}}}\right) < 1.05,
 \end{aligned} \tag{16}$$

where  $|\mathbf{d}|$  is the number of valid pixels in ground truth depth maps.

## B. Additional Experimental Result

Qualitative comparison on real-world benchmarks is reported in Fig. 10. We further compare existing methods on geometric accuracy by back-projecting the estimated depth to 3D point clouds. The results on NYUv2 and ScanNet are reported in Fig. 11 and Fig. 12, respectively.

## C. Limitation and Future Work

While the proposed framework demonstrates robust performance, it is currently optimized specifically for the depth super-resolution task. However, the broader field of depth perception encompasses several critical challenges that remain outside the scope of this study, such as depth estimation, which focuses on inferring high-quality depth maps solely from monocular imagery, and depth completion, which targets the recovery of dense depth information from sparse, non-uniform measurements generated by LiDAR sensors, ToF cameras, or Structure-from-Motion (SfM) pipelines. Developing a unified foundational model capable of addressing these diverse depth-related problems simultaneously holds significant practical value for real-world applications in robotics and autonomous systems. Consequently, bridging the gap between various depth-related problems within a generalized architecture represents a primary direction for our future research.